

Multiwavelength Modeling of the Luminous Fast Blue Optical Transient AT2024wpp

Conor M. B. Omand¹*, Nikhil Sarin^{2,3}, Gavin P. Lamb¹, Daniel A. Perley¹, Andrew Mummery⁴, Hamid Hamidani⁵, Steve Schulze⁶, Emma R. Beasor¹, Aleksandra Bochenek¹, Helena-Margaret S. Grabham¹, Sorcha R. Kennelly¹, Nguyen M. Khang¹, Shiho Kobayashi¹, Genevieve Schroeder⁷, William N. Stone¹, Cairns Turnbull¹, Jacob Wise¹

¹Astrophysics Research Institute, Liverpool John Moores University, Liverpool Science Park IC2, 146 Brownlow Hill, Liverpool, UK, L3 5R

²Kavli Institute for Cosmology, University of Cambridge, Madingley Road, CB3 0HA, UK

³Institute of Astronomy, University of Cambridge, Madingley Road, CB3 0HA, UK

⁴School of Natural Sciences, Institute for Advanced Study, 1 Einstein Drive, Princeton, NJ 08540, USA

⁵Astronomical Institute, Graduate School of Science, Tohoku University, Sendai 980-8578, Japan

⁶Center for Interdisciplinary Exploration and Research in Astrophysics (CIERA), Northwestern University, 1800 Sherman Ave., Evanston, IL 60201, USA

⁷Department of Astronomy, Cornell University, Ithaca, NY 14853, USA

Accepted XXX. Received YYY; in original form ZZZ

ABSTRACT

Luminous fast blue optical transients (LFBOTs) are a growing class of enigmatic energetic transients. They show fast rises and declines, high temperatures throughout their evolution, and non-thermal emission in radio and X-rays. Their power source is currently unknown, but proposed models include engine-driven supernovae, interaction-powered supernovae, shock cooling emission, intermediate mass black hole tidal disruption events (IMBH TDEs), and Wolf-Rayet/black hole mergers, among others. AT2024wpp is the most optically luminous LFBOT to date and has been observed extensively at multiple wavelengths, including radio, optical, UV, and X-rays. We take models from multiple scenarios and fit them to the AT2024wpp optical, radio, and X-ray light curves to determine if which of these scenarios can best describe all aspects of the data. We show that none of the multiwavelength light curve models can reasonably explain the data, although other physical arguments favour a stellar mass/IMBH TDE of a low mass star and a synchrotron blast wave. We discuss how this scenario can be tested with late-time observations, and what other scenarios could possibly explain the broadband data.

Key words: transients: supernovae – transients: tidal disruption events – stars: black holes

1 INTRODUCTION

Recent high-cadence wide-field surveys, such as the Zwicky Transient Facility (ZTF, Bellm et al. 2019a) and the Asteroid Terrestrial-impact Last Alert System (ATLAS, Tonry 2011; Tonry et al. 2018), have led to the discovery and characterization of several new types of fast optical transients (Drout et al. 2014; Arcavi et al. 2016; Pursiainen et al. 2018; Ho et al. 2023b). These transients evolve faster than typical supernovae (SNe) and can have peak luminosities similar to superluminous supernovae (SLSNe, Gal-Yam 2012; Nicholl 2021; Gomez et al. 2024). These properties rule out typical ^{56}Ni -powered core-collapse or thermonuclear SN models, since the mass of ^{56}Ni required to explain the luminosity would be larger than the mass of the ejected material (Perley et al. 2019; Margutti et al. 2019). Further studies have shown that many of these transients are likely Type Ibn/Icn SNe (Ho et al. 2023b); SNe powered by the interaction between the ejected material and circumstellar material (CSM). However, a few of the more luminous fast optical transients have shown multi-component multiwavelength signatures consistent with a cen-

tral engine (Margutti et al. 2019; Ho et al. 2019, 2020, 2022; Metzger 2022a; Chrimis et al. 2024b); these transients have become known as luminous fast blue optical transients (LFBOTs).

The prototype LFBOT is AT2018cow (‘the Cow’, Prentice et al. 2018), the closest observed event so far ($z = 0.014$). The optical emission rose to peak within ~ 2.5 days, and peaked at an absolute magnitude ~ -20.5 . The optical spectra had only a few broad features, indicating expansion velocities $\gtrsim 0.1c$ and temperatures $\sim 30\,000$ K. Around 15 days, the spectrum began to show H and He features at velocities $\sim 3000 - 4000$ km s $^{-1}$, but showed no evidence of cooling to normal late-time SN temperatures (Margutti et al. 2019; Perley et al. 2019; Xiang et al. 2021). The spectrum also showed narrow emission components ($v \lesssim 300$ km s $^{-1}$), consistent with CSM interaction (Fox & Smith 2019; Dessart et al. 2021). The Cow showed polarization of $\sim 7\%$ at 5.7d post-explosion, which quickly faded to show no polarization after 8 days except for a $\lesssim 1$ day increase to $\sim 1.5\%$ in the blue at 13 days (Smith et al. 2018; Maund et al. 2023). Follow-up observations also found a persistent UV source coincident with the Cow at \sim years post-explosion (Sun et al. 2022, 2023; Chen et al. 2023a,b; Inkenhaag et al. 2023, 2025).

The Cow was also bright at other wavelengths. Soft X-ray emis-

* E-mail: c.m.omand@ljmu.ac.uk

sion was detected shortly after the explosion (Rivera Sandoval et al. 2018; Kuin et al. 2019), and followed a shallow temporal decline until steepening at ~ 20 days, when the optical lines at $\sim 3000 - 4000$ km s^{-1} emerged (Margutti et al. 2019). The soft X-ray light curve was highly variable, and quasi-periodic oscillations (QPOs) were claimed at 225 Hz (Pasham et al. 2021) and 4 mHz (Xiang et al. 2021), giving constraints on the mass of the central object to be $< 850 M_\odot$ and $10^3 - 10^5 M_\odot$, respectively. The persistent source found at \sim years post-explosion also showed soft X-ray emission (Migliori et al. 2024). The Cow also showed bright hard X-ray, radio, and millimetre emission (Ho et al. 2019; Margutti et al. 2019; Nayana & Chandra 2021). The radio evolved smoothly and showed a steep temporal drop at ~ 1 month (Ho et al. 2019), indicating a different origin from the X-rays. The atypical properties of the radio compared to radio SNe can be understood if the radiating electrons have a relativistic Maxwellian energy distribution (Ho et al. 2022; Margalit & Quataert 2021, 2024).

The multiwavelength analysis from Margutti et al. (2019) found that that observed properties of the Cow can be explained by a central engine surrounded by an aspherical ejecta with a trans-relativistic polar component and a lower velocity equatorial ring or torus. The central engine hypothesis for LFBOTs is also supported by the time variability of the X-rays, giant optical flares from AT2022tsd (Ho et al. 2023a), possible QPOs, and long-lasting UV/X-ray remnant. The radio emission is likely caused by the interaction between the trans-relativistic component and surrounding high density (10^5 cm^{-3}), wind-like CSM (Margutti et al. 2019; Ho et al. 2019) on scales of $\sim 10^{16} \text{ cm}$. For wind speeds of $\sim 1000 \text{ km s}^{-1}$ (typical of Wolf-Rayet stars), the mass loss rate is implied to be $\dot{M} = 10^{-4} - 10^{-3} M_\odot \text{ yr}^{-1}$ (Margutti et al. 2019), which is more than an order of magnitude higher than expected in Wolf-Rayet stars (Barlow et al. 1981; Nugis & Lamers 2000; Adhyaqs et al. 2020). This indicates either an extended CSM or a distinct physical origin (Fox & Smith 2019). In the early phase, the optical emission from the polar component is thought to arise from reprocessed X-ray emission from the central engine (Piro & Lu 2020; Uno & Maeda 2020a; Calderón et al. 2021; Chen & Shen 2022; Uno & Maeda 2023). The photosphere from this component recedes into the equatorial torus as reprocessing becomes less efficient on the timescale where the lower velocity lines emerge.

Since the discovery of the Cow, a few other transients have been discovered with similar properties. These include AT2018lug/ZTF18abvkwla ('the Koala', Ho et al. 2020), CSS161010 (Coppejans et al. 2020; Gutiérrez et al. 2024), AT2020xnd/ZTF20acigmel ('the Camel', Perley et al. 2021; Bright et al. 2022; Ho et al. 2022), AT2020mrf (Yao et al. 2022), AT2022tsd ('the Tasmanian Devil', Matthews et al. 2023; Ho et al. 2023a), and AT2023fhn ('the Finch', Chrimes et al. 2024a,b). These objects show some variety in peak luminosity and ejecta velocity, but all show hot, roughly featureless early spectra, optical luminosities similar to SLSNe, and bright X-ray and radio emission. Somalwar et al. (2025) also discovered AT2024puz, which has similar properties to both LFBOTs and TDEs and evolves on a timescale intermediate between the two. The LFBOT rate is estimated to be $< 0.1\%$ of the core-collapse SN rate (Ho et al. 2023b), and they normally occur in metal-poor, low-mass starburst galaxies (Ho et al. 2019; Michałowski et al. 2019; Coppejans et al. 2020; Lyman et al. 2020; Yao et al. 2022). These environments are similar to those of Type-I SLSN and long gamma-ray burst (GRB) progenitors (Lunnan et al. 2014; Chen et al. 2015; Leloudas et al. 2015; Angus et al. 2016; Chen et al. 2017; Schulze et al. 2018; Ørum et al. 2020), which may indicate that these transients all come from massive, low-metallicity progenitors.

Although the ejecta structure of LFBOTs is somewhat understood, the nature of the progenitor that produces it is still unknown. A few proposed scenarios include engine-driven SNe (e.g. Prentice et al. 2018; Liu et al. 2022; Omand & Sarin 2024), failed SNe with prompt accretion disc formation (Margutti et al. 2019; Perley et al. 2019; Quataert et al. 2019), tidal disruption events (TDEs) from intermediate mass black holes (IMBHs, Perley et al. 2019; Kuin et al. 2019), choked jets (Gottlieb et al. 2022; Soker 2022; Suzuki & Maeda 2022; Suzuki et al. 2024; Hamidani et al. 2025b), highly aspherical SNe ('ellipsars', DuPont et al. 2022), and the merger of a compact object and massive star (Lyutikov & Toonen 2019; Uno & Maeda 2020a; Schröder et al. 2020; Metzger 2022a). CSM-interaction models have also been proposed (Fox & Smith 2019; Xiang et al. 2021; Pellegrino et al. 2022; Khatami & Kasen 2024), but these are disfavoured due to the variability and long duration of the X-ray emission. The central X-ray source could be either a magnetized nebula (e.g. Omand et al. 2018; Vurm & Metzger 2021; Omand et al. 2025b), which can cause ejecta asymmetry due to Rayleigh-Taylor instabilities between the wind and ejecta (Blondin & Chevalier 2017; Suzuki & Maeda 2017, 2021; Omand et al. 2025a); the inner region of a Super-Eddington accretion disc (Sadowski & Narayan 2015); or a choked jet (Gottlieb et al. 2022). The transients can be infrared bright due to the dense outflow creating a light echo (Metzger & Perley 2023; Li et al. 2025) or from newly formed dust reprocessing emission from the central engine (Omand et al. 2019).

One of the newest additions to the LFBOT class is AT2024wpp ('the Whippet' Ho et al. 2024). AT2024wpp is one of the closest ($z = 0.0868$, Perley et al. 2024) and brightest ($L_{\text{bol,peak}} > 10^{45} \text{ erg s}^{-1}$) LFBOTs to date, and the first one to be identified before the optical/UV peak (Ho et al. 2024). A comprehensive multiwavelength dataset on the object has been collected, including NIR/optical/UV photometry and spectroscopy, optical polarization, radio and millimetre data, and X-ray data (Srinivasaragavan et al. 2024; Margutti et al. 2024; Schroeder et al. 2024; Pursiainen et al. 2025; Nayana et al. 2025; LeBaron et al. 2025; Perley et al. 2026). AT2024wpp is featureless at early epochs, but shows weak H and He features after ~ 30 days. Late-time observations show no evidence for minute-timescale flares similar to AT2022tsd (Ofek et al. 2025). The optical peak is well described by a $\gtrsim 30\,000 \text{ K}$ blackbody, and the optical component remains well-described by a $\gtrsim 20\,000 \text{ K}$ blackbody out to late times, although there is some evidence for a power-law NIR excess after ~ 20 days. The X-ray emission hardens over time and shows a rebrightening at ~ 50 days. The radio emission rises quickly over $\sim 20\text{--}30$ days before starting to decline.

This work attempts to find a physically plausible scenario for AT2024wpp that can explain both the thermal and non-thermal emission. We approach this task by fitting several semi-analytic models to each component and using the results of those fits to determine whether different scenarios are viable. We summarize the data we attempt to model in Section 2 and the models used in Section 3. The results are shown in Section 4 and discussed in Section 5. Finally, we conclude in Section 6.

2 DATA MODELED

The data we model include the NIR/optical/UV photometry, radio data, and X-ray data presented in (Perley et al. 2026). The photometry was gathered using a number of surveys and facilities, including the Zwicky Transient Facility (ZTF; Bellm et al. 2019b; Graham et al. 2019; Dekany et al. 2020) using the Samuel Oschin 48-inch Schmidt telescope, IO:O and the Liverpool Infra-Red Imaging Cam-

Model	REDBACK Model Name	Reference
<i>Optical</i>		
Evolving Blackbody	evolving_blackbody	Sarin et al. (2024)
^{56}Ni -powered SN	arnett	Arnett (1982)
Magnetar-powered SN	general_magnetar_driven_supernova	Sarin et al. (2022); Omand & Sarin (2024)
CSM-powered SN	csm_nickel	Chatzopoulos et al. (2013); Villar et al. (2017); Jiang et al. (2020)
Fallback-powered SN	sn_nickelFallback	Guillochon et al. (2018)
SN + Envelope Shock Cooling	shockcooling_sapirwaxman_and_arnett	Sapir & Waxman (2017)
SN + CSM Shock Cooling	shock_cooling_and_arnett	Piro et al. (2021)
Cocoon + Envelope Shock Cooling	shocked_cocoon_and_arnett	Piro & Kollmeier (2018)
Cocoon + CSM Shock Cooling	shocked_cocoon_csm_and_arnett	Hamidani et al. (2025a,b)
Fallback TDE	tdeFallback	Guillochon & Ramirez-Ruiz (2013); Guillochon et al. (2018); Mockler et al. (2019)
Stream-Stream Collision TDE	stream_stream_tde	Piran et al. (2015); Ryu et al. (2020)
Cooling Envelope TDE	gaussianrise_cooling_envelope	Metzger (2022b); Sarin & Metzger (2024)
BH-WR Merger	wr-bh_merger	Metzger (2022a)
<i>Radio and X-ray</i>		
Top-hat Jet	tophat_redback	Lamb et al. (2018)
Gaussian Jet	gaussian_redback	Lamb et al. (2018)
Power-Law Synchrotron	synchrotron_pldensity	Rosswog & Brüggen (2007); Chevalier & Fransson (2017)
Thermal Synchrotron	thermal_synchrotron_v2_fluxdensity	Margalit & Quataert (2021, 2024)
Accretion Disc	fitted	Mummary & Balbus (2020); Mummary et al. (2024a,b)
Top-hat Jet + Accretion Disc	tophat_redback & fitted	

Table 1. The optical, radio, and X-ray models used to fit the data for AT2024wpp, and their associated references.

era (LIRIC) on the Liverpool Telescope, the Rainbow Palomar 60-inch telescope at Palomar Observatory, the Panoramic Survey Telescope and Rapid Response System (Pan-STARRS), Goodman High-Throughput Spectrograph (GHTS) on the Southern Astrophysical Research Telescope (SOAR), the ESO Faint Object Spectrograph and Camera v2 (EFOSC2) on the New Technology Telescope (NTT), the Focal Reducer/Low Dispersion Spectrograph 2 (FORS2) on the Very Large Telescope (VLT), the Ultraviolet-Optical Telescope (UVOT) on the Neil Gehrels *Swift* Observatory, and the Wide Field Camera 3 (WFC3) on the Hubble Space Telescope (HST). X-ray observations were taken by the X-Ray Telescope (XRT) on *Swift*, and the radio observations were taken by the Karl G. Jansky Very Large Array (VLA) and Atacama Large Millimetre/submillimetre Array (ALMA). Overall, the UVOIR photometric data has detections spanning ~ 120 days and upper limits at $\sim 150 - 220$ days after the last detection. The radio data spans the 3.0 – 350 GHz frequency range and has detections up to ~ 200 days post-discovery. The X-ray data is only in one band (0.2 – 10 keV), and lasts ~ 80 days. Upper limits were not included in model fits in either the optical or non-thermal models, although late-time upper limits are used as constraints in Section 5.

3 MODELS AND FITTING

We test various models by performing Bayesian inference to fit them to the multiband optical photometry and radio data using REDBACK (Sarin et al. 2024). We use the PyMULTINEST sampler (Buchner et al. 2014) implemented in BILBY (Ashton et al. 2019), and sample in flux density with a Gaussian likelihood. We use the default priors implemented in REDBACK for all models unless otherwise specified; these priors are wide enough that posteriors converging to the edge of the prior is not an issue. We sample the initial time with a uniform prior of up to 20 days before the first observation, and include a host ex-

inction term A_V with a uniform prior between 0 and 2 mag for the optical data. A list of the models used is given in Table 1.

The first model used is a evolving blackbody model, which fits the transient by assuming the photospheric temperature and radius both have power-law rises and declines in time. The temperature and radius peaks are not assumed to be at the same time. While this will not reveal the physics of the LFBOT, it will allow us to characterize the photospheric radius and temperature of the system, which can provide insight into the properties that the more physical models need to have in order to describe the data..

The physical semi-analytic optical models we test can be divided into a few broad classes: SNe, shock cooling, TDEs, and stellar mergers. These models were chosen to represent the wide range of phenomena that could potentially explain LFBOTs. These models all calculate the bolometric luminosity and photospheric radius of one or more components, and convert that to observed emission by assuming each component is described by a blackbody spectral energy distribution.

We test four SN models, which differ depending on their power source. One is the standard ^{56}Ni -powered SN, known as the Arnett model (Colgate & McKee 1969; Arnett 1982). This model usually has difficulty explaining transients with high luminosities and low diffusion times, due to the constraint that the ^{56}Ni mass must be lower than the ejecta mass. The other SNe models also have ^{56}Ni , but are primarily powered by a different source. One model is the millisecond magnetar model (Omand & Sarin 2024), which was shown in Omand & Sarin (2024) to be a good fit to the LFBOT ZTF20acigmel ('the Camel', Perley et al. 2021). Another is the CSM interaction model (Chatzopoulos et al. 2013; Villar et al. 2017; Jiang et al. 2020), powered by the conversion of kinetic energy into luminosity via the shock formed between the ejecta and CSM. The final one is the fallback SN model (Guillochon et al. 2018), which is powered by the accretion of material onto a central black hole remnant.

Shock cooling emission is the radiation from shock heated mate-

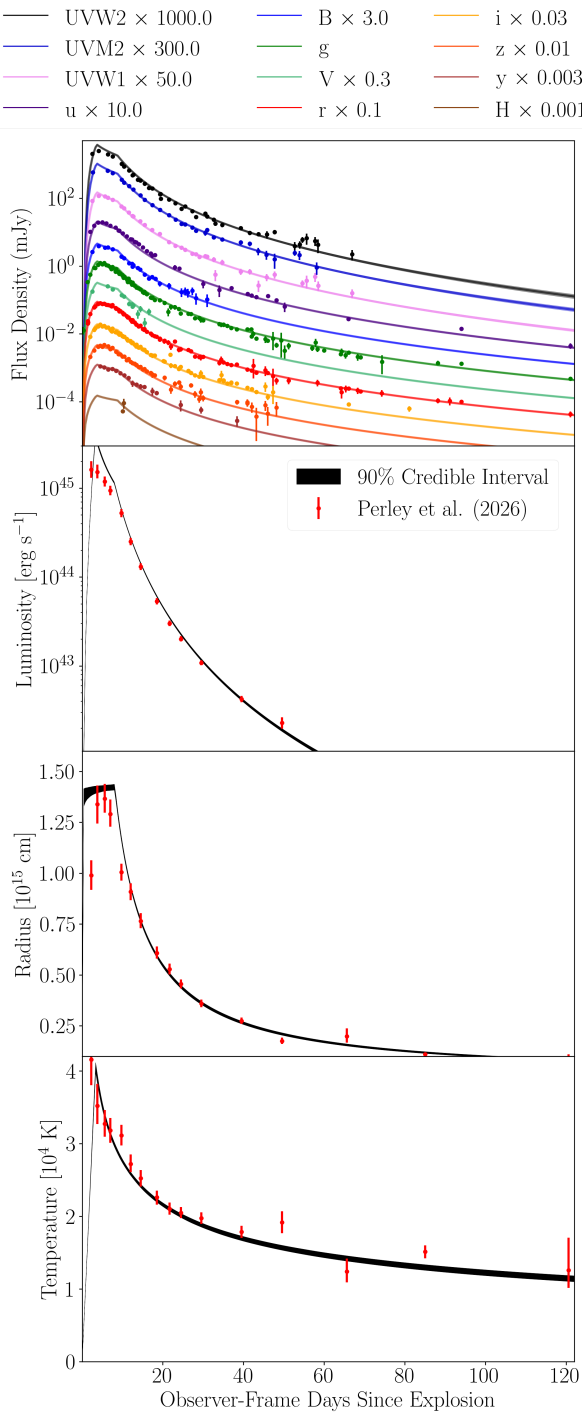


Figure 1. The multiband fit from the evolving blackbody (top) and the luminosity (second), radius (third), and temperature (bottom) derived from it. The shaded region shows the 90% credible interval. Values from Perley et al. (2026) are shown in red.

rial as it cools and expands after shock breakout (e.g. Margalit 2022). The shock that heats the material can come from either an SN explosion or a GRB jet, leaving a region of shocked material called the cocoon. The material can either be the envelope of the star or an extended CSM. This leads us to examine four shock cooling scenarios: the SN + envelope (Sapir & Waxman 2017), SN + extended CSM (Piro et al. 2021), cocoon + envelope (Piro & Lu 2020), and cocoon

+ extended CSM (Hamidani et al. 2025a,b). Shock cooling can emit on short timescales but cannot produce emission at later times, so we test all the shock cooling models alongside a ^{56}Ni component to better explain late-time emission.

We test three models for TDE emission, which vary how the optical emission is produced after the star is disrupted. None of the models self-consistently solve the early pre-circularization emission, and instead they all assume a constant-temperature Gaussian rise until peak. The first model assumes the emission is directly powered by fallback accretion onto the central black hole (Guillochon & Ramirez-Ruiz 2013; Guillochon et al. 2018; Mockler et al. 2019). The second model assumes the emission is powered by shocks resulting from the collisions of debris streams (Piran et al. 2015; Ryu et al. 2020). The final TDE model assumes the bound debris forms a quasi-steady envelope which cools radiatively as it undergoes Kelvin-Helmholtz contraction (Metzger 2022b; Sarin & Metzger 2024). For these models, we alter the default prior such that the lower bound of the black hole mass goes down to $10^3 M_\odot$, since the TDE rise time is predominately set by the black hole mass and a timescale of ~ 5 days requires an intermediate mass black hole.

The final optical model is the disruption and hyper-accretion of a Wolf-Rayet star onto a black hole companion, with a delay between the common envelope phase and the merger (Metzger 2022a). The optical emission in this model is primarily powered by reprocessed X-rays from the inner accretion disc, although interaction between ejecta and CSM can also contribute at later times.

To try and explain the radio and X-ray emission, we test models from GRB afterglows, CSM interaction from non-relativistic or trans-relativistic spherical blast waves, and from an accretion disc. Since previous LFBOTs have shown evidence for multiple components in their non-thermal emission, the radio and X-ray data are fit separately. We test two jet structures for the afterglow: a top-hat jet and a Gaussian jet (Lamb et al. 2018). For CSM interaction, we test a pure synchrotron model (Rosswog & Brüggen 2007; Chevalier & Fransson 2017) and a thermal synchrotron model (Margalit & Quataert 2021, 2024). The GRB afterglow models are assumed to be in a constant density medium since they decelerate further away from the progenitor, while the interaction models are assumed to be in a medium with a power-law density profile $\rho \propto r^{-\alpha}$, with α between 0 and 4. The emission from the accretion disc is fit using models from FitTED (Mummery et al. 2024a) imported into REDBACK, and we also examine a case with a jet and accretion disc.

4 RESULTS

4.1 Optical

Figure 1 shows the multiband fit from the evolving blackbody model and the luminosity, photospheric radius, and temperature derived from it; the values found by Perley et al. (2026) are also shown as a comparison. The model provides a good fit to the overall, showing that a blackbody with power-law time dependence can approximate the system well. The inferred luminosities, radii, and temperatures also broadly agree with other measurements from LeBaron et al. (2025). The radius increase with power-law index $\sigma_{R,\text{rise}} = 0.01^{+0.01}_{-0.01}$ and decreases with $\sigma_{R,\text{decline}} = -1.06^{+0.01}_{-0.01}$, while the temperature rises with $\sigma_{T,\text{rise}} = 1.02^{+0.01}_{-0.01}$ and declines with $\sigma_{T,\text{decline}} = -0.35^{+0.01}_{-0.01}$, where R or $T \propto t^\sigma$. The luminosity indices are determined from R or T , which give an initial rise index of $4.10^{+0.06}_{-0.06}$, an intermediate decline index of $-1.38^{+0.06}_{-0.06}$, then a final decline index of $-3.52^{+0.06}_{-0.06}$. The inferred luminosities, radii, and temperatures do

differ from [Perley et al. \(2026\)](#) at early, likely due to the simplified power-law time evolution of those properties in our model, so inferred parameters during the early and intermediate phases are likely unreliable.

Figure 2 shows the fits to the optical data with the more physically-motivated models. Several models, including the magnetar-powered SN model, SN + envelope shock cooling model, and black hole-Wolf Rayet (BH-WR) merger model, can reproduce the main properties of the light curve well. A few other models, including the nickel-powered and fallback-powered SN models as well as the cocoon + envelope and SN + CSM shock cooling models, can somewhat reproduce the data but underpredict the UV emission around peak. The TDE models all fail to describe the data, with the fallback model evolving much too slowly, and the stream-stream collision and cooling envelope models having their Gaussian rises producing emission up to ~ 20 days, which is far longer than the rise time from the data of ~ 5 days.

The parameters for each of the SN, shock cooling, and BH-WR merger models all contain a plateau temperature, T_{floor} , which has a wide prior between 10^3 and 10^5 K. Models with this parameter keep the photospheric temperature at a minimum value T_{floor} at late times, resulting in the photospheric radius receding as the luminosity continues to decrease. This allows the models to approximate a time when the photosphere recedes without the need to continuously calculate the optical depth of the ejecta. [Nicholl et al. \(2017\)](#) mention that this parameter may contain information about other processes keeping the ejecta at a constant temperature, such as recombination or ejecta fragmentation from a central engine. Using T_{floor} also allows the model to make multiband predictions deep into the nebular phase, when the photosphere no longer exists. Since emission at this phase is driven mostly by line emission, a blackbody approximation can not make accurate predictions past the photospheric phase (see discussion in [Schulze et al. 2024](#)).

The values of T_{floor} from the fits shown in Figure 2 are between 20 000 – 40 000 K, similar to the values found for the LFBOT ZTF20acigmel by [Omand & Sarin \(2024\)](#). This is much higher than the ~ 5000 K that has been estimated for other transients ([Nicholl et al. 2017; Taddia et al. 2019](#)). This implies the photosphere begins to recede early, which is consistent with the data. However, this also implies that the ejecta becomes optically thin within $\lesssim 10$ days (see Appendix A), which is not consistent with the spectroscopic data ([Perley et al. 2026](#)).

We re-fit the optical data with the same models, but with the upper limit on the prior for T_{floor} set to 10^4 K - these fits are shown in Figure 3. $T_{\text{floor}} \leq 10^4$ K was chosen because it is below the inferred late-time temperature of the LFBOT (Figure 1), so a model would have to self-consistently calculate the photospheric radius and temperature to explain the data. The TDE models do not use T_{floor} , and thus remain unchanged. Most models now cool to $\leq 10^4$ K on timescales comparable to the peak of the LFBOT or earlier, and fail to reproduce the UV data. Only the magnetar-driven SN model and BH-WR merger model can reproduce the light curve peak, but cool down shortly after and fail to reproduce the observed decline, again underpredicting the UV data.

4.2 Radio and X-ray

Figure 4 shows the fits to the radio and X-ray data, which were modelled separately to allow for the possibility that they could arise from separate processes. The radio data are better reproduced by the two afterglow models and the power-law synchrotron blast wave model compared to the thermal synchrotron blast wave model. Specifically,

the afterglows and power-law synchrotron show a more pronounced peak on the same timescale as the data and a faster decline, although none of the models can reproduce the fast decline consistent with the 3 GHz upper limit. The jets are both predicted to be strongly off-axis, with $\theta_{\text{obs}}/\theta_{\text{core}} \sim 5 - 10$. The power-law synchrotron is predicted to be in a medium with $\rho \propto r^{-2.9}$. The fits to the X-ray data show a different preference; the synchrotron blast wave models reproduce the later data well but underpredict the early data, while the jet and accretion disc models fail to reproduce the data entirely, especially at late times.

An important consideration from the radio and X-ray fits is what they predict for the opposite band, since a model that overpredicts the other band would not be a viable candidate. Figure 5 shows the fits presented in Figure 4 extended into the opposite band. The two jet models and power-law synchrotron model from the X-ray data all have wide confidence intervals that roughly overlap with the radio data, while the thermal synchrotron model overpredicts the radio data and the accretion disc and jet + accretion disc models underpredict. The models that are consistent with the radio data show very different behaviours in the X-ray, with the Gaussian jet severely underpredicting the data; thermal synchrotron being consistent with the late data but underpredicting the early data; the top-hat jet being roughly consistent but showing a rise on the timescale of 25 days, which is not observed; and the power-law synchrotron model overpredicting the data by an order of magnitude.

Putting these results together yields no obvious explanation for the non-thermal emission. The radio could be explained by an off-axis Gaussian jet, since the X-ray flux of that model does not overpredict the data. The X-ray flux is only consistent with the synchrotron models, but the thermal synchrotron overpredicts the radio data. The power-law synchrotron models from the X-ray fits are roughly consistent with the radio data, yet the models from the radio fits overpredict the X-ray data by more than an order of magnitude. If the X-rays are powered by a power-law synchrotron blast wave, there may be emission from a second component, like an off-axis jet, that can better reproduce the early radio emission, but that component would need to have a radio flux not significantly larger than the blast wave and a negligible X-ray flux.

The two possibilities to explain the non-thermal emission that arise from our analysis, assuming that the data are not described by a model we have not investigated, are that a power-law synchrotron blast wave can explain both the radio and X-ray data, or that a combined Gaussian jet and power-law synchrotron blast wave are needed to explain the data. We show the combined radio and X-ray fits for both of these scenarios in Figure 6. The power-law synchrotron fit is similar to the fits presented in Figure 4: The model underpredicts X-rays at early times but reproduces the data at late times, and does not reproduce the peak or the decline in the radio data. The synchrotron + Gaussian jet model reproduces the peak and decline in the radio data, but underpredicts the X-ray data. Since neither of these possibilities can explain the data, we conclude that the radio and X-ray emission were produced by a process we have not considered here.

5 DISCUSSION

5.1 Model Analysis and Late-Time Predictions

The optical models tested all failed to reproduce the optical emission unless the temperature was allowed to plateau at $> 20 000$ K. This highlights the need for multiband fitting when examining light curve models, as opposed to bolometric fitting. After the diffusion phase,

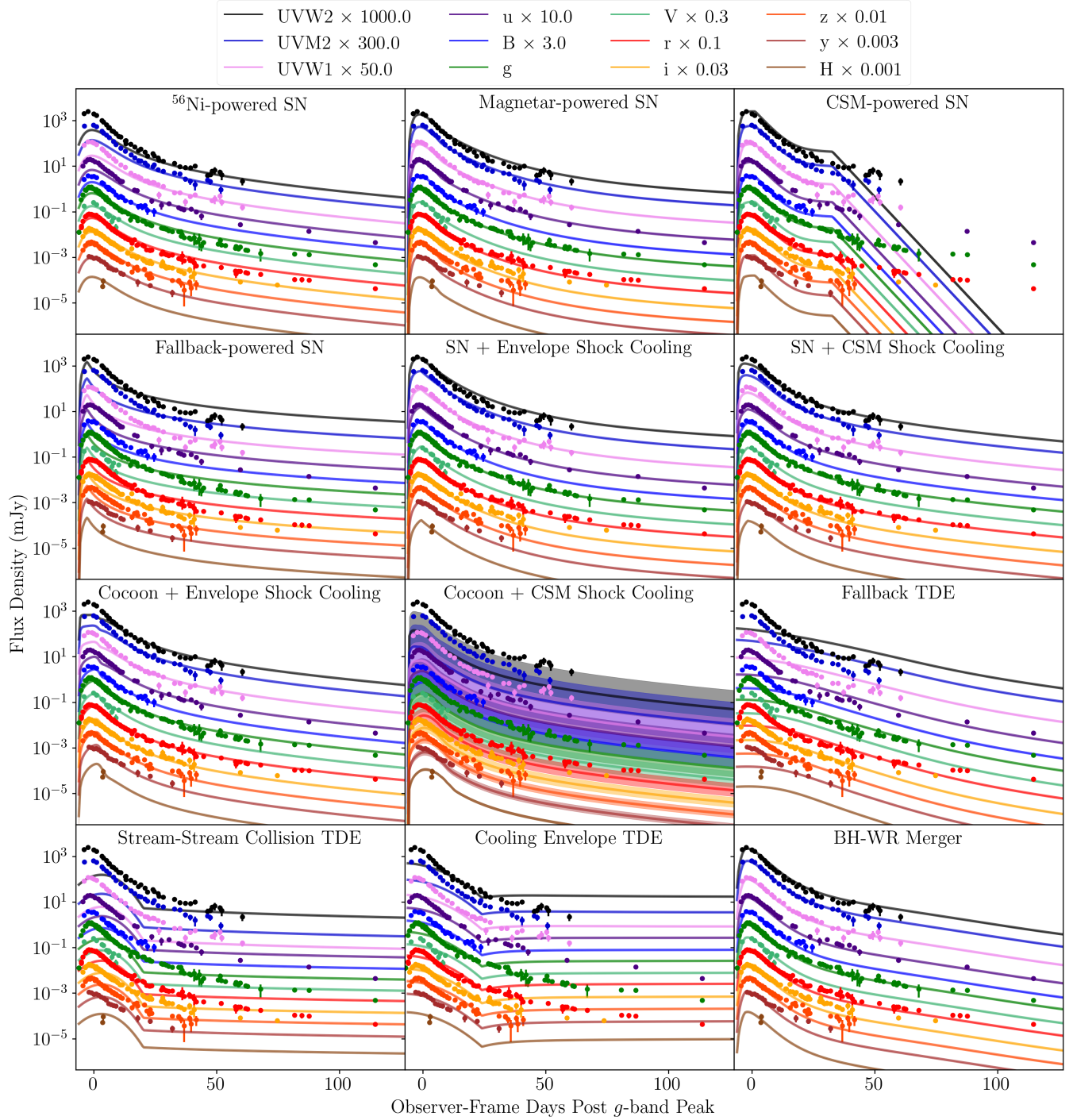


Figure 2. The light curve fits to the broadband optical data for each model discussed in Section 3 (see Table 1) using default priors. The solid line shows the model with the highest likelihood while the shaded region shows the 90% confidence interval.

a constant temperature implies $L \propto R_{\text{phot}}^2$, which may be a good approximation when the photosphere is receding. The recession of the photosphere in an expanding medium begins when the optical depth of the ejecta drops fast enough to counteract the effect of the ejecta expansion. This timescale can be connected to the nebular timescale, when the entire ejecta becomes optically thin. Appendix A shows that the ratio between these two timescales for a homologously expand-

ing medium with any non-increasing density profile is $< \sqrt{3}$. While the data show the photospheric radius peaks on a timescale of ~ 5 days, spectra at ~ 40 days still show the emission being dominated by a blackbody-like continuum (Perley et al. 2026). Since this is inconsistent with the derived timescales, this suggests that the ejecta responsible for the thermal emission cannot be homologously expanding, which rules out the SN, shock cooling, and BH-WR merger

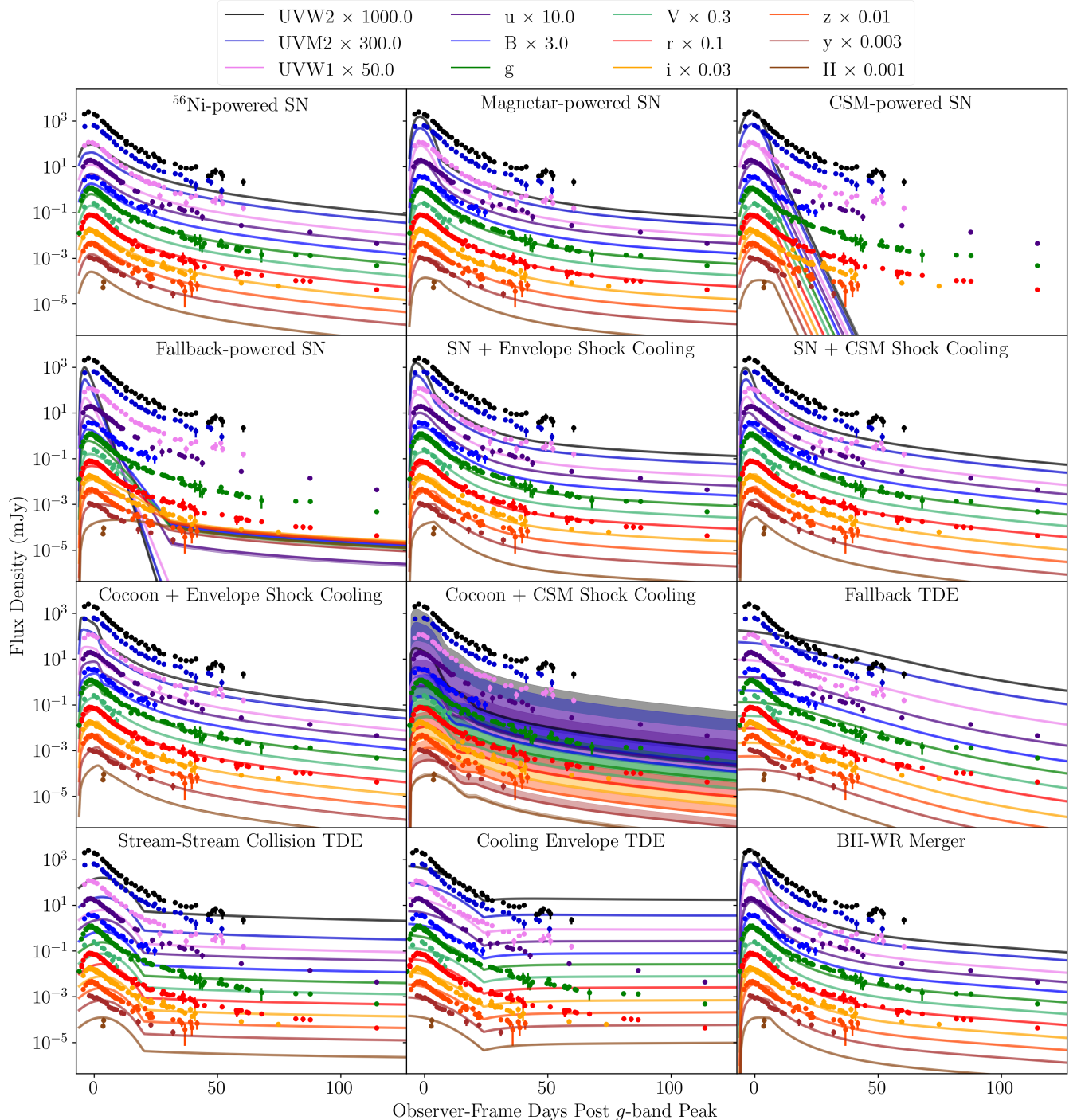


Figure 3. Same as Figure 2, but with the prior for T_{floor} restricted to $< 10^4$ K.

models. This can also rule out some models we did not test, such as the TDE-powered SN model from [Tsuna & Lu \(2025\)](#) or the Helium core-black hole merger from [Klencki & Metzger \(2025\)](#). This does not rule out the presence of homologous components that may produce spectral lines or non-thermal emission, but these components cannot be the primary source of the optical emission. This photospheric behaviour also does not rule out TDEs, although none of the TDE models were able to explain the optical emission. However,

TDE models are known to be uncertain and the emission processes of supermassive black hole (SMBH) TDEs, especially around peak are not well understood (e.g. [Sarin & Metzger 2024](#); [Wise et al. 2025](#)), so the possibility that this transient could be an IMBH TDE cannot be completely discounted. The lack of early rest-frame optical/near-UV spectral features may point to AT2024wpp as a low mass analogue to featureless TDEs ([Hammerstein et al. 2023](#)).

One way of testing models is using their early properties to predict

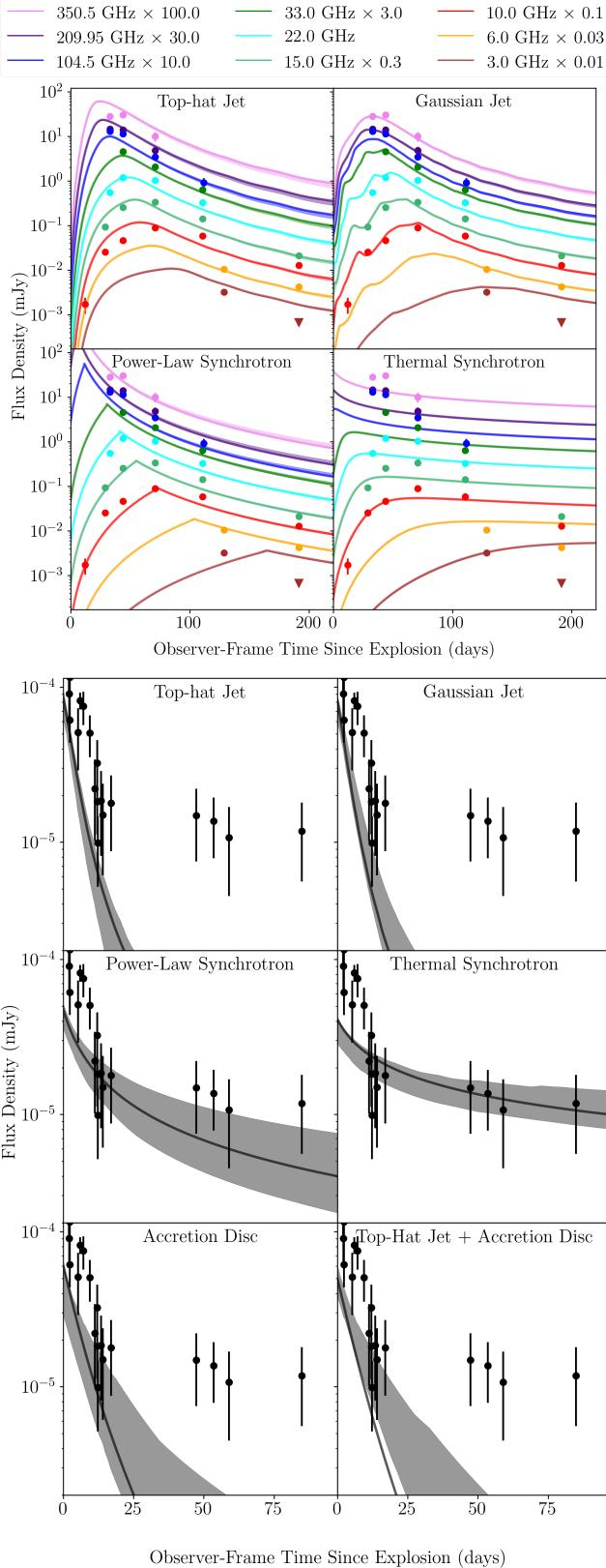


Figure 4. The light curve fits to the radio and submillimetre (top) and X-ray (bottom) data for each model discussed in Section 3 (see Table 1). The solid line shows the model with the highest likelihood while the shaded region shows the 90% confidence interval.

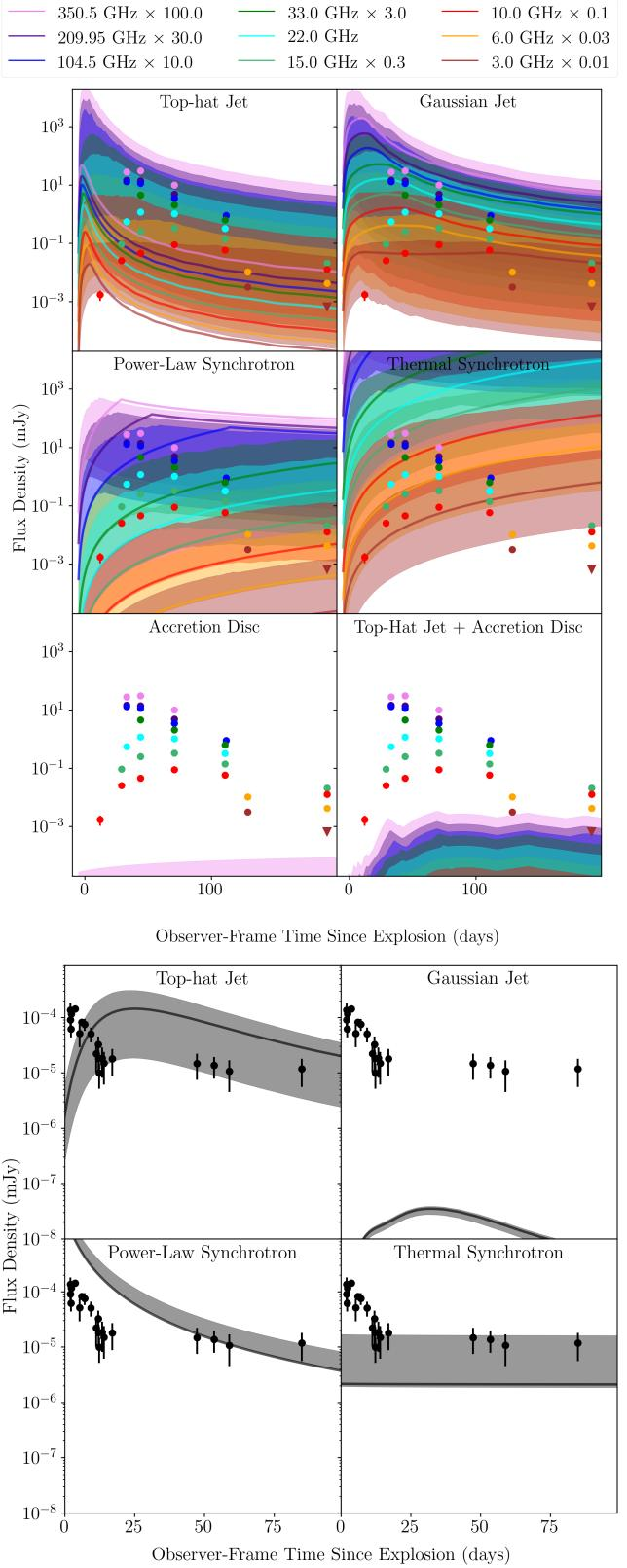


Figure 5. Radio light curves using the posteriors from the X-ray fits (top) and X-ray light curves using the radio posteriors (bottom) (see Figure 4 for the fits). The shaded region shows the 90% confidence intervals, while the solid line shows the model with the highest likelihood from the original fits.

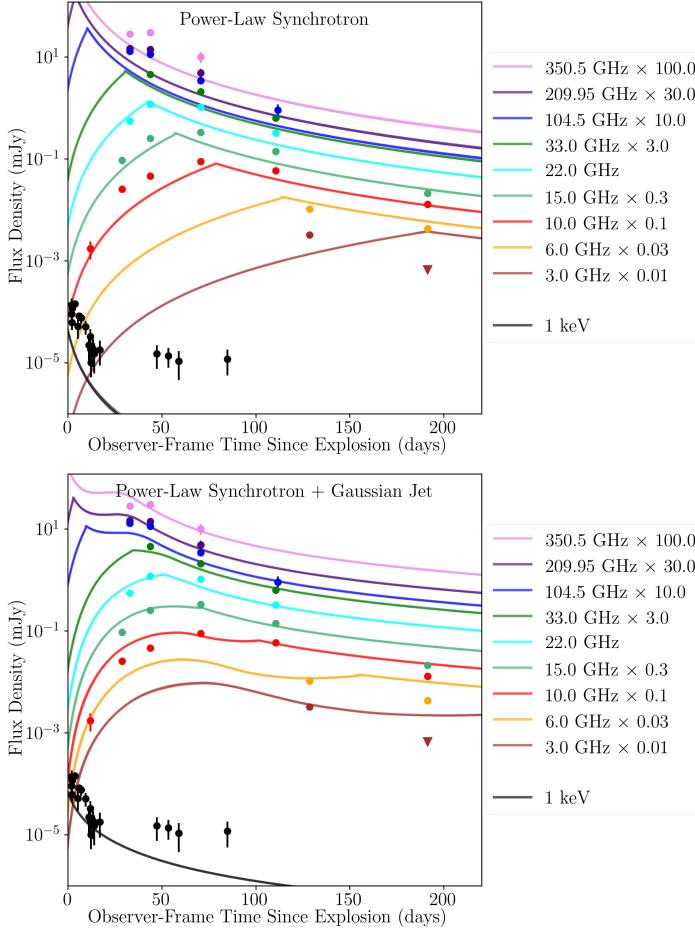


Figure 6. The light curve fits to the radio, submillimetre, and X-ray data for the power-law synchrotron (top) and thermal synchrotron (bottom) models. The solid line shows the model with the highest likelihood while the shaded region shows the 90% confidence interval.

emission at later times (e.g. Law et al. 2019; Omand & Jerkstrand 2023; Margutti et al. 2023). The late-time emission from tidal disruption events can be predicted in radio (e.g. Zauderer et al. 2011; van Velzen et al. 2016; Andreoni et al. 2022; Alexander et al. 2025), infrared (e.g. Dou et al. 2016; Newsome et al. 2024; Masterson et al. 2024), X-rays (e.g. Bade et al. 1996; Donley et al. 2002; Grotova et al. 2025), and may also be in neutrinos (e.g. Stein et al. 2021; Jiang et al. 2023; Ji et al. 2025; Toshikage et al. 2025). One prediction from all TDE models is that the system will settle into an accretion disc at late times, which will emit primarily in optical/UV and X-rays (Mummery et al. 2024a). Since the TDE models for early optical emission did not reproduce the data for AT2024wpp, we do not use the posteriors from those models for predictions. We instead present F225W UV and 1 keV predictions¹ for 10^3 and $10^5 M_\odot$ black holes and 0.5 and $5.0 M_\odot$ accretion discs in Figure 7. These black hole

¹ These predictions were made using the GR_disc model from FirTeD (Mummery et al. 2024a), which ignores relativistic photon deflection and gravitational redshift. Marginalizing over a prior using a model incorporating these effects (GR_disc_plus) would be computationally unfeasible. These effects are not expected to strongly affect optical/UV emission, but may introduce uncertainty in the X-ray predictions.

masses were chosen because the plateau emission from AT2018cow was estimated to originate from a $\sim 10^3 M_\odot$ black hole (Inkenhaag et al. 2023, 2025), with $10^5 M_\odot$ acting as a conservative upper limit. The observer-inclination angle and black hole spin are marginalized over using their default priors (Mummery et al. 2024a), while the initial disc radius r_0 and viscous timescale t_{visc} are calculated via

$$r_0 = 2R_\star (M_{\text{BH}}/2M_{\text{disc}})^{1/3} \quad (1)$$

and

$$t_{\text{visc}} = \mathcal{V} \sqrt{r_0^3/GM_{\text{BH}}}. \quad (2)$$

We use the mass-radius relation $R_\star = (M_\star/M_\odot)^{4/5} R_\odot$ appropriate for lower-mass main sequence stars (Metzger 2022b; Sarin & Metzger 2024), and the parameter \mathcal{V} encapsulates the poorly understood MHD effects in the disc physics. We sample \mathcal{V} with a log-uniform prior between 10^2 and 10^4 . Shown also are 3σ upper limits from Perley et al. (2026).

The F225W predictions have ~ 3 mag of uncertainty, with the $10^5 M_\odot$ black holes having emission between 22–26th mag and the $10^3 M_\odot$ black holes having emission between 26–30th mag, making it likely this emission could be detected if the black hole mass is close to the IMBH-SMBH boundary, but more parameter dependent if the black hole mass is lower. The X-ray predictions have \gtrsim an order of magnitude of uncertainty, especially during the first year, but are predicted to be between $\sim 10^{-1} - 10^{-5}$ mJy over the next two years. More massive black holes and discs have higher early uncertainty but higher luminosity at late times. The HST UV upper limit disfavours black holes with masses $\gtrsim 10^5 M_\odot$, but does not strongly constrain discs around lower mass black holes. The *Swift* X-ray upper limit at ~ 1 year strongly disfavours these all of these plateau models, which suggests either a lower mass disc or black hole, or that AT2024wpp is not an IMBH TDE.

The late-time optical, UV, and X-ray upper limits can be used to exclude some regions of the $M_{\text{BH}} - M_{\text{disc}}$ parameter space through modelling of the plateau emission in the case of an IMBH TDE – this is shown in Figure 8 for all upper limits at > 200 days, including limits from the VLT, HST, and *Swift*. We sample a log-uniform prior for both M_{BH} and M_{disc} , with M_{BH} ranging from $1 - 10^5 M_\odot$ and M_{disc} ranging from $0.05 - 10 M_\odot$. The upper limit for the M_{BH} prior is because any larger black hole would cause the initial transient to be too slow, and the lower limit on disc mass prior was chosen so we could examine tidal disruptions of the lowest mass stars. We calculate r_0 and t_{visc} using Equations 1 and 2, and all other parameters use their default priors. Disc masses $\gtrsim 1 M_\odot$ are excluded with 99% confidence for a black hole mass of $> 10^2 M_\odot$. At 90% confidence, disc masses $\gtrsim 0.3 M_\odot$ are excluded for a black hole mass of $> 10^2 M_\odot$. Black hole masses of $\gtrsim 10^{4.5}$ and $\gtrsim 10^4 M_\odot$ are excluded for all disc masses at 99% and 90% confidence respectively. However, we caution against drawing too strong a conclusion from a posterior based only on a few upper limits.

5.2 Other Scenarios

Metzger (2022a) outlined several progenitor scenarios for LFBOTs, including engine-powered SNe (e.g. Prentice et al. 2018), pulsational pair instability SNe (PPISNe, e.g. Leung et al. 2021), prompt collapse from failed SNe or PPISNe (e.g. Margutti et al. 2019), IMBH TDEs (e.g. Quataert et al. 2019; Perley et al. 2019; Margutti et al. 2019), stellar mass BH TDEs (e.g. Perets et al. 2016; Kremer et al. 2019,

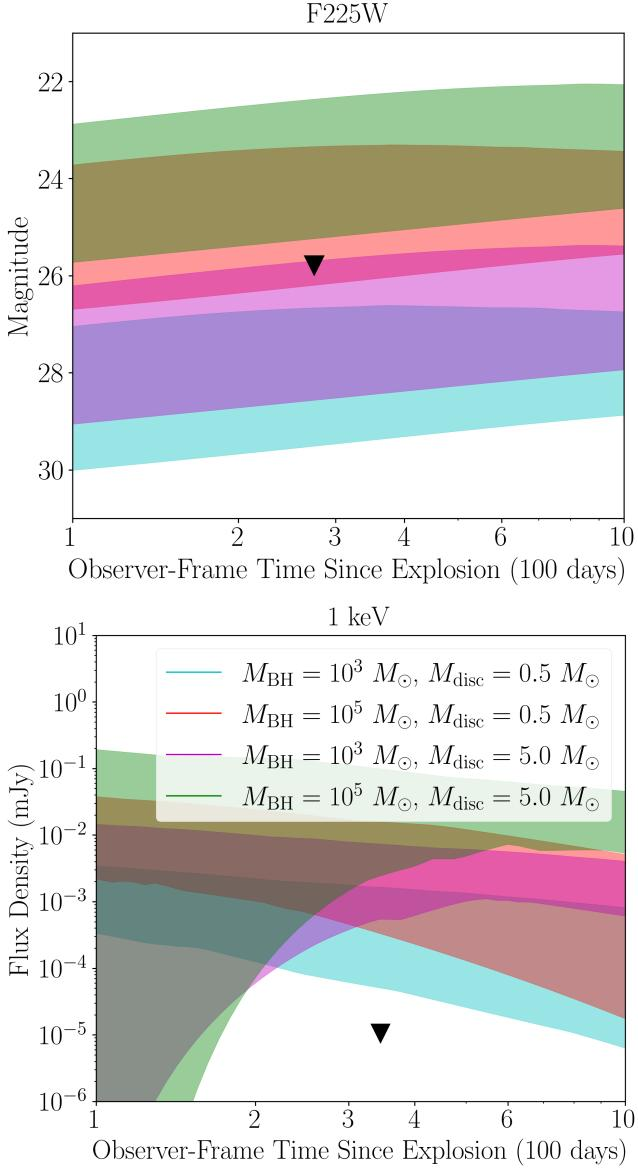


Figure 7. The predicted late-time emission from the accretion disc of an IMBH TDE. Each colour represents a different black hole mass and disc mass, while the width of the band shows the 90% confidence interval from marginalizing over the default priors for the other parameters (see Mummery et al. (2024a) for details). The top panel shows the prediction for F225W, while the bottom panel shows the predictions at 1 keV. The triangles denote the observed 3σ upper limits.

2023; Beniamini et al. 2025), failed common envelope with a prompt merger (e.g. Soker 2019; Soker et al. 2019; Schröder et al. 2020), and failed common envelope with a delayed merger (e.g. Metzger 2022a). This work examined engine-driven SNe and TDEs, while PPISNe and current failed common envelope models are not supported by the photospheric radius timescales derived in Appendix A.

Failed SNe remain an intriguing possibility, though predicting their optical signatures is extremely challenging (Beasor et al. 2024), as theoretical models offer a wide range of predictions for what a failed SN might look like. Different models of failed SNe have predicted no observable signature (Kochanek et al. 2008), a long-lived infrared transient with little to no optical emission (Lovegrove &

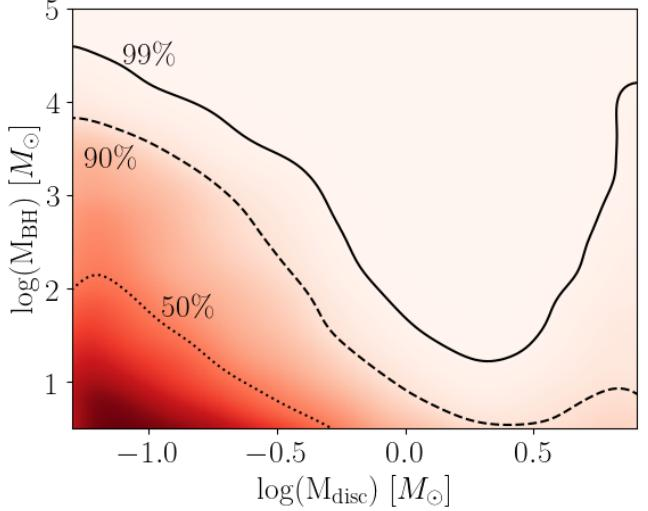


Figure 8. The viable region for plateau emission given the late-time UV and X-ray upper limits in an IMBH TDE. The darker regions indicate a high posterior density. The dotted, dashed, and solid lines indicate parameter regions excluded at 50%, 90%, and 99% confidence.

Woosley 2013), a long-lived optical transient (Perna et al. 2014), or even a short-lived relatively bright transient (Antoni & Quataert 2023; Antoni et al. 2025), similar to an LFBOT. Chrimes et al. (2025) examine the possibility of failed SNe from very massive stars ($> 30 M_\odot$), similar to the progenitors of super-kilonovae (Siegel et al. 2022), and find that the rates, host metallicities, mass loss rates, and expected plateau emission roughly match with the LFBOT population and previous observations. In this case, LFBOTs may contribute significantly to r-process enrichment in galaxies.

Although there are no reliable models for the optical flare from a prompt collapse failed SN, the system should settle into an accretion disc at later times, similar to TDEs. The expected plateau emission for failed SNe involving high and low mass stars are shown in Figure 9. The priors are similar to the IMBH TDE plateaus, except the initial disc radius r_0 is calculated by assuming the progenitor star is maximally rotating and the angular momentum of the black hole J_{BH} is much less than the angular momentum of the disc J_{disc} . These assumptions give a radius

$$r_0 = 2R_\star \left(\frac{M_\star}{M_{\text{disc}}} \right)^2 \left(\frac{M_\star}{M_{\text{BH}}} \right), \quad (3)$$

with $M_\star = M_{\text{disc}} + M_{\text{BH}}$. It is worth noting that this calculation ignores the self-gravity of the disc, which can be important when $M_{\text{disc}} \gtrsim M_{\text{BH}}$. The F225W emission has ~ 3 mag of uncertainty and is fainter than the IMBH TDE plateau, and the observed upper limit is not constraining. The X-ray emission is predicted to be fainter than 10^{-2} mJy but have lots of uncertainty, except for the $M_{\text{disc}} = M_{\text{BH}} = 50 M_\odot$ case. The X-ray upper limit disfavours discs $\gtrsim 50 M_\odot$ but does not constrain black hole mass. Sampling the prior to find the excluded area in the failed SN scenario, as done with TDEs in Figure 8, does not give meaningful constraints on either the black hole or disc mass.

Another scenario of interest is a reprocessing outflow, where an accretion disc powers an outflow that reprocesses the disc emission, powering an optical transient (Piro & Lu 2020). Models of these outflows have successfully reproduced previous TDEs (Uno & Maeda 2020b; Matsumoto & Piran 2021) and LFBOTs (Uno &

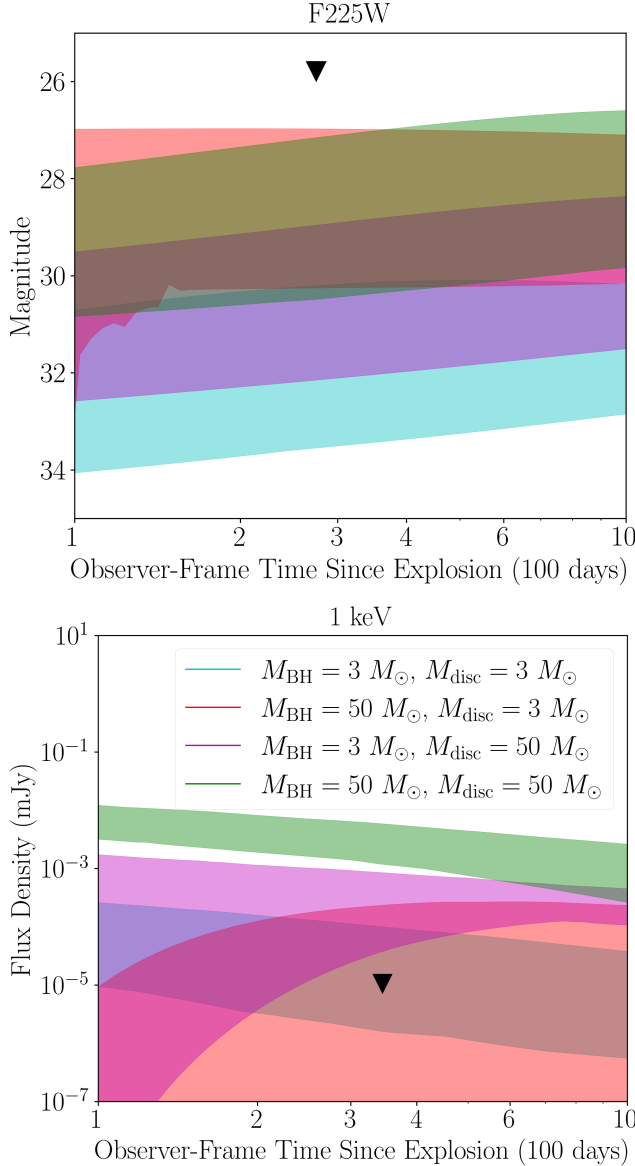


Figure 9. Same as Figure 7, but for discs resulting from failed SNe.

Maeda 2020a, 2023). The continuous mass injection of the model means that even though the outflow is expanding, the properties of the photospheric radius cannot be described by the relations in Appendix A. The photospheric radius will expand outward initially with the outflow until it reaches the radius where the outer region of the outflow is too diffuse to absorb light, and its recession is governed by the time-dependence of the mass outflow rate, with the outflow becoming optically thin only when the outflow rate becomes sufficiently small. This should lead to an early photospheric peak and a late nebular phase, which is observed in AT2024wpp. Both Piro & Lu (2020) and Uno & Maeda (2020a) predict an increase in photospheric temperature after a short time, contrary to what is observed, but this could be due to simplifications in their models. A calculation of the X-ray opacity within this model would be useful to predict when the emission from the accretion disc will escape unattenuated.

5.3 Summary of Previous Interpretations

Our analysis of AT2024wpp and our interpretation of the event is mostly in broad agreement with previous studies. LeBaron et al. (2025) and Perley et al. (2026) both concluded that a homologously expanding medium can not explain the optical transient, and preferred a reprocessing outflow model similar to that discussed above, although no attempts were made to compare a model light curve to the data. LeBaron et al. (2025) also discuss a dense CSM interaction model (Khatami & Kasen 2024) as well as BH-WR merger and TDE-powered SN models (Metzger 2022a; Tsuna & Lu 2025), ruling out the former and but not the latter two.

The density profile and density from our modelling of the radio emission with a power-law synchrotron blast wave were $n_{\text{CSM}} \propto r^{-2.9}$ and $n_{\text{CSM}} \approx 10^7 \text{ cm}^{-3}$ at 10^{16} cm respectively, which match well with the shock modelling from Nayana et al. (2025) and Perley et al. (2026). Those works find that the shock radius recedes after ~ 100 days, something which is not accounted for in any of our models and can explain the discrepancy at late times. They also both point out that these CSM properties seem to be typical of LFBOTs as well as some interacting SNe, such as the Type Ibn SN 2006jc (Maeda & Moriya 2022). This may imply similar progenitors for the two systems, as previously suggested by Metzger (2022a) and Klencki & Metzger (2025).

LeBaron et al. (2025) observe an excess of IR emission after ~ 20 –30 days, which was not well described by Perley et al. (2026) due to a lack of late-time IR observations. This excess is similar to the one observed in AT2018cow (Perley et al. 2019; Margutti et al. 2019), although it emerges at a later timescale. Two models that can explain the IR excess are free-free opacity effects, which require several solar masses of outflow (Chen & Shen 2022), and a dust echo (Metzger & Perley 2023), which reproduces the emission with densities similar to those inferred from the radio emission. As noted by LeBaron et al. (2025), this means the radio and IR emission can form in the same medium by completely separate processes.

Nayana et al. (2025) found that the X-ray rebrightening and spectral steepening can be explained by a Compton bump, and posit that the timescale may be due to a drop in the X-ray opacity due to ionization breakout (Metzger et al. 2014; Metzger & Piro 2014) at ~ 40 days. This also roughly corresponds to the timescale at which the broad features disappear from the optical spectrum (Perley et al. 2026). The appearing and disappearing features are expected in a reprocessing outflow model, as the early medium should be hot and ionized until enough material has been expelled, then should remain partially ionized at the photosphere until the photosphere recedes into the ionized region (analogous to a Strömgren sphere) caused by the inner X-ray source. Nayana et al. (2025) favour a model with super-Eddington accretion onto a compact object which produces aspherical disc-wind outflows. The polarization measurements by Pur- siainen et al. (2025) seem to prohibit large scale asymmetries in the outflow, although small-scale clumping can produce a polarization signal below the observed noise threshold (e.g. Tanaka et al. 2017).

Finally, Perley et al. (2026) used scaling relations (Mummery et al. 2024b) to get a black hole mass constraint from the late-time non-detections of a plateau. They find a black hole mass limit of $3 \times 10^4 M_{\odot}$, similar to what we infer at 99% confidence from Figure 8.

6 SUMMARY AND CONCLUSIONS

In this work, we examined the optical, radio, and X-ray emission from the LFBOT AT2024wpp. The data were compared to a num-

ber of models to try and determine which physical scenario can best explain the transient. A few optical models, including the magnetar-powered SN model, SN + envelope and SN + CSM shock cooling models, and BH-WR merger model, can reproduce the optical data if the temperature of the model plateaus above 20 000 K. This is not unphysical but does imply that the ejecta should become optically thin on a much faster timescale than what is suggested by the spectroscopic data (Perley et al. 2026). While GRB afterglow models and synchrotron blast wave models can explain the radio and X-ray emission separately, a combination of these models fails to adequately explain the non-thermal emission from the system.

Analysis of the behaviour of the photospheric radius disfavours models featuring a homologously expanding ejecta. Although the TDE models were not able to reproduce the data, we do not rule out this scenario due to the uncertainty of the emission mechanism in the stellar-mass/IMBH regime. The late-time optical emission from the accretion disc is likely undetectable unless the black hole mass is almost supermassive, but X-rays may be detectable for the first several years. Current constraints favour the disruption of a low-mass star from a black hole with either intermediate or stellar mass.

AT2024wpp could be a failed SN with prompt black hole formation, but there are no reliable models for the optical flare in order to test the scenario. A failed SN would have an accretion disc that would also be detectable in X-rays and display different behaviour than accretion discs from IMBH TDEs, allowing the scenarios to be differentiated. A reprocessing wind may be able to explain the optical emission, and opacity calculations from that model would be useful for predicting late X-ray emission from the disc.

ACKNOWLEDGEMENTS

The authors would like to thank Kim Page for her help with *Swift* data and Ashley Chrimes for helpful discussions. CMBO, GPL, and CT acknowledge support from the Royal Society (grant Nos. DHF-R1-221175 and DHF-ERE-221005). NS acknowledges support from the Kavli Foundation. NMK acknowledges support from LIV.INNO (STFC grant ST/W006766/1). ERB is supported by a Royal Society Dorothy Hodgkin Fellowship (grant no. DHF-R1-241114).

DATA AVAILABILITY

All data used are publicly available from Perley et al. (2026). All models used are publicly available within REDBACK (Sarin et al. 2024).

REFERENCES

Adhyaqa A., Malasan H. L., Aprilia et al. 2020, in Journal of Physics Conference Series. IOP, p. 012001, doi:10.1088/1742-6596/1523/1/012001

Alexander K. D., Margutti R., Gomez S., et al. 2025, arXiv e-prints, p. arXiv:2506.12729

Andreoni I., Coughlin M. W., Perley D. A., et al. 2022, *Nature*, 612, 430

Angus C. R., Levan A. J., Perley D. A., et al. 2016, *MNRAS*, 458, 84

Antoni A., Quataert E., 2023, *MNRAS*, 525, 1229

Antoni A., Jiang Y.-F., Quataert E., 2025, arXiv e-prints, p. arXiv:2509.16308

Arcavi I., Wolf W. M., Howell D. A., et al. 2016, *ApJ*, 819, 35

Arnett W. D., 1980, *ApJ*, 237, 541

Arnett W. D., 1982, *ApJ*, 253, 785

Arnett W. D., Fu A., 1989, *ApJ*, 340, 396

Ashton G., Hübner M., Lasky P. D., et al. 2019, *ApJS*, 241, 27

Bade N., Komossa S., Dahlem M., 1996, *A&A*, 309, L35

Barlow M. J., Smith L. J., Willis A. J., 1981, *MNRAS*, 196, 101

Beasor E. R., Hosseinzadeh G., Smith N., et al. 2024, *ApJ*, 964, 171

Bellm E. C., Kulkarni S. R., Graham M. J., Dekany R., et al. 2019a, *PASP*, 131, 018002

Bellm E. C., Kulkarni S. R., Graham M. J., et al. 2019b, *PASP*, 131, 018002

Beniamini P., Perets H. B., Granot J., 2025, arXiv e-prints, p. arXiv:2509.22779

Blondin J. M., Chevalier R. A., 2017, *ApJ*, 845, 139

Bright J. S., Margutti R., Matthews D., et al. 2022, *ApJ*, 926, 112

Buchner J., Georgakakis A., Nandra K., et al. 2014, *A&A*, 564, A125

Calderón D., Pejcha O., Duffell P. C., 2021, *MNRAS*, 507, 1092

Chatzopoulos E., Wheeler J. C., Vinko J., et al. 2013, *ApJ*, 773, 76

Chen C., Shen R.-F., 2022, *Research in Astronomy and Astrophysics*, 22, 035017

Chen T. W., Smartt S. J., Jerkstrand A., et al. 2015, *MNRAS*, 452, 1567

Chen T.-W., Smartt S. J., Yates R. M., et al. 2017, *MNRAS*, 470, 3566

Chen Y., Drou M. R., Piro A. L., et al. 2023a, *ApJ*, 955, 42

Chen Y., Drou M. R., Piro A. L., et al. 2023b, *ApJ*, 955, 43

Chevalier R. A., Fransson C., 2017, in Alsabti A. W., Murdin P., eds., Hand-book of Supernovae. p. 875, doi:10.1007/978-3-319-21846-5_34

Chrimes A. A., Jonker P. G., Levan A. J., et al. 2024a, *MNRAS*, 527, L47

Chrimes A. A., Coppejans D. L., Jonker P. G., et al. 2024b, *A&A*, 691, A329

Chrimes A. A., Jonker P. G., Levan A. J., et al. 2025, arXiv e-prints, p. arXiv:2510.03402

Colgate S. A., McKee C., 1969, *ApJ*, 157, 623

Coppejans D. L., Margutti R., Terreran G., et al. 2020, *ApJ*, 895, L23

Dekany R., Smith R. M., Riddle R., et al. 2020, *PASP*, 132, 038001

Dessart L., Hillier D. J., Sukhbold T., et al. 2021, *A&A*, 656, A61

Donley J. L., Brandt W. N., Eracleous M., et al. 2002, *AJ*, 124, 1308

Dou L., Wang T.-g., Jiang N., et al. 2016, *ApJ*, 832, 188

Drou M. R., Chornock R., Soderberg A. M., et al. 2014, *ApJ*, 794, 23

DuPont M., MacFadyen A., Zrake J., 2022, *ApJ*, 931, L16

Fox O. D., Smith N., 2019, *MNRAS*, 488, 3772

Gal-Yam A., 2012, *Science*, 337, 927

Gomez S., Nicholl M., Berger E., et al. 2024, *MNRAS*, 535, 471

Gottlieb O., Tchekhovskoy A., Margutti R., 2022, *MNRAS*, 513, 3810

Graham M. J., Kulkarni S. R., Bellm E. C., et al. 2019, *PASP*, 131, 078001

Grotova I., Rau A., Baldini P., et al. 2025, *A&A*, 697, A159

Guillochon J., Ramirez-Ruiz E., 2013, *ApJ*, 767, 25

Guillochon J., Nicholl M., Villar V. A., et al. 2018, *ApJS*, 236, 6

Gutiérrez C. P., Mattila S., Lundqvist P., et al. 2024, *ApJ*, 977, 162

Hamidani H., Sato Y., Kashiyama K., Tanaka M., Ioka K., Kimura S. S., 2025a, *ApJ*, 986, L4

Hamidani H., Ioka K., Kashiyama K., Tanaka M., 2025b, *ApJ*, 988, 30

Hammerstein E., van Velzen S., Gezari S., et al. 2023, *ApJ*, 942, 9

Ho A. Y. Q., Phinney E. S., Ravi V., et al. 2019, *ApJ*, 871, 73

Ho A. Y. Q., Perley D. A., Kulkarni S. R., et al. 2020, *ApJ*, 895, 49

Ho A. Y. Q., Margalit B., Bremer M., et al. 2022, *ApJ*, 932, 116

Ho A. Y. Q., Perley D. A., Chen P., et al. 2023a, *Nature*, 623, 927

Ho A. Y. Q., Perley D. A., Gal-Yam A., et al. 2023b, *ApJ*, 949, 120

Ho A. Y. Q., Srinivasaragavan G., Perley D., et al. 2024, Transient Name Server AstroNote, 272, 1

Inkenhaag A., Jonker P. G., Levan A. J., et al. 2023, *MNRAS*, 525, 4042

Inkenhaag A., Levan A. J., Mummery A., et al. 2025, *MNRAS*, 544, L108

Ji S., Wang Z., Zhu L., et al. 2025, arXiv e-prints, p. arXiv:2508.09408

Jiang B., Jiang S., Ashley Villar V., 2020, *Research Notes of the American Astronomical Society*, 4, 16

Jiang N., Zhou Z., Zhu J., et al. 2023, *ApJ*, 953, L12

Khatami D. K., Kasen D. N., 2024, *ApJ*, 972, 140

Klencki J., Metzger B. D., 2025, arXiv e-prints, p. arXiv:2510.09745

Kochanek C. S., Beacom J. F., Kistler M. D., et al. 2008, *ApJ*, 684, 1336

Kremer K., Lu W., Rodriguez C. L., et al. 2019, *ApJ*, 881, 75

Kremer K., Mockler B., Piro A. L., et al. 2023, *MNRAS*, 524, 6358

Kuin N. P. M., Wu K., Oates S., et al. 2019, *MNRAS*, 487, 2505

Lamb G. P., Mandel I., Resmi L., 2018, *MNRAS*, 481, 2581

Law C. J., Omand C. M. B., Kashiyama K., et al. 2019, *ApJ*, 886, 24

LeBaron N., Margutti R., Chornock R., et al. 2025, arXiv e-prints, p. arXiv:2509.00951

Leloudas G., Schulze S., Krühler T., et al. 2015, *MNRAS*, **449**, 917

Leung S.-C., Fuller J., Nomoto K., 2021, *ApJ*, **915**, 80

Li J.-Y., Yu Y.-W., Liu L.-D., et al. 2025, arXiv e-prints, p. [arXiv:2504.19897](https://arxiv.org/abs/2504.19897)

Liu J.-F., Zhu J.-P., Liu L.-D., et al. 2022, *ApJ*, **935**, L34

Lovegrove E., Woosley S. E., 2013, *ApJ*, **769**, 109

Lunnan R., Chornock R., Berger E., et al. 2014, *ApJ*, **787**, 138

Lyman J. D., Galbany L., Sánchez S. F., et al. 2020, *MNRAS*, **495**, 992

Lyutikov M., Toonen S., 2019, *MNRAS*, **487**, 5618

Maeda K., Moriya T. J., 2022, *ApJ*, **927**, 25

Margalit B., 2022, *ApJ*, **933**, 238

Margalit B., Quataert E., 2021, *ApJ*, **923**, L14

Margalit B., Quataert E., 2024, *ApJ*, **977**, 134

Margutti R., Metzger B. D., Chornock R., et al. 2019, *ApJ*, **872**, 18

Margutti R., Bright J. S., Matthews D. J., et al. 2023, *ApJ*, **954**, L45

Margutti R., J. N. A., Chornock R., et al. 2024, Transient Name Server AstroNote, **339**, 1

Masterson M., De K., Panagiotou C., et al. 2024, *ApJ*, **961**, 211

Matsumoto T., Piran T., 2021, *MNRAS*, **502**, 3385

Matthews D., Margutti R., Metzger B. D., et al. 2023, *Research Notes of the American Astronomical Society*, **7**, 126

Maund J. R., Höflich P. A., Steele I. A., et al. 2023, *MNRAS*, **521**, 3323

Metzger B. D., 2022a, *ApJ*, **932**, 84

Metzger B. D., 2022b, *ApJ*, **937**, L12

Metzger B. D., Perley D. A., 2023, *ApJ*, **944**, 74

Metzger B. D., Piro A. L., 2014, *MNRAS*, **439**, 3916

Metzger B. D., Vurm I., Hascoët R., et al. 2014, *MNRAS*, **437**, 703

Michałowski M. J., Kamphuis P., Hjorth J., et al. 2019, *A&A*, **627**, A106

Migliori G., Margutti R., Metzger B. D., et al. 2024, *ApJ*, **963**, L24

Mockler B., Guillochon J., Ramirez-Ruiz E., 2019, *ApJ*, **872**, 151

Mummery A., Balbus S. A., 2020, *MNRAS*, **492**, 5655

Mummery A., Nathan E., Ingram A., et al. 2024a, arXiv e-prints, p. [arXiv:2408.15048](https://arxiv.org/abs/2408.15048)

Mummery A., van Velzen S., Nathan E., et al. 2024b, *MNRAS*, **527**, 2452

Nayana A. J., Chandra P., 2021, *ApJ*, **912**, L9

Nayana A. J., Margutti R., Wiston E., et al. 2025, arXiv e-prints, p. [arXiv:2509.00952](https://arxiv.org/abs/2509.00952)

Newsome M., Arcavi I., Howell D. A., et al. 2024, *ApJ*, **961**, 239

Nicholl M., 2021, *Astronomy and Geophysics*, **62**, 5.34

Nicholl M., Guillochon J., Berger E., 2017, *ApJ*, **850**, 55

Nugis T., Lamers H. J. G. L. M., 2000, *A&A*, **360**, 227

Ofek E. O., Ozer L., Konno R., et al. 2025, arXiv e-prints, p. [arXiv:2508.18359](https://arxiv.org/abs/2508.18359)

Omand C. M. B., Jerkstrand A., 2023, *A&A*, **673**, A107

Omand C. M. B., Sarin N., 2024, *MNRAS*, **527**, 6455

Omand C. M. B., Kashiyama K., Murase K., 2018, *MNRAS*, **474**, 573

Omand C. M. B., Kashiyama K., Murase K., 2019, *MNRAS*, **484**, 5468

Omand C. M. B., Sarin N., Temim T., 2025a, *MNRAS*, **536**, 408

Omand C. M. B., Sarin N., Lamb G. P., 2025b, *MNRAS*, **539**, 1908

Ørum S. V., Ivens D. L., Strandberg P., et al. 2020, *A&A*, **643**, A47

Pasham D. R., Ho W. C. G., Alston W., et al. 2021, *Nature Astronomy*, **6**, 249

Pellegrino C., Howell D. A., Vinkó J., et al. 2022, *ApJ*, **926**, 125

Perets H. B., Li Z., Lombardi Jr. J. C., et al. 2016, *ApJ*, **823**, 113

Perley D. A., Mazzali P. A., Yan L., et al. 2019, *MNRAS*, **484**, 1031

Perley D. A., Ho A. Y. Q., Yao Y., et al. 2021, *MNRAS*, **508**, 5138

Perley D. A., Qin Y., Rich R. M., et al. 2024, Transient Name Server AstroNote, **280**, 1

Perley D. A., Ho A. Y. Q., McGrath Z., et al. 2026, arXiv e-prints, p. [arXiv:2601.01999](https://arxiv.org/abs/2601.01999)

Perna R., Duffell P., Cantiello M., et al. 2014, *ApJ*, **781**, 119

Piran T., Svirski G., Krolik J., et al. 2015, *ApJ*, **806**, 164

Piro A. L., Kollmeier J. A., 2018, *ApJ*, **855**, 103

Piro A. L., Lu W., 2020, *ApJ*, **894**, 2

Piro A. L., Haynie A., Yao Y., 2021, *ApJ*, **909**, 209

Prentice S. J., Maguire K., Smartt S. J., et al. 2018, *ApJ*, **865**, L3

Pursiainen M., Childress M., Smith M., et al. 2018, *MNRAS*, **481**, 894

Pursiainen M., Killestein T. L., Kuncarayakti H., et al. 2025, *MNRAS*, **537**, 3298

Quataert E., Lecoanet D., Coughlin E. R., 2019, *MNRAS*, **485**, L83

Rivera Sandoval L. E., Maccarone T. J., Corsi A., et al. 2018, *MNRAS*, **480**, L146

Rosswog S., Brüggen M., 2007, Introduction to High-Energy Astrophysics

Ryu T., Krolik J., Piran T., 2020, *ApJ*, **904**, 73

Sapir N., Waxman E., 2017, *ApJ*, **838**, 130

Sarin N., Metzger B. D., 2024, *ApJ*, **961**, L19

Sarin N., Omand C. M. B., Margalit B., et al. 2022, *MNRAS*, **516**, 4949

Sarin N., Hübner M., Omand C. M. B., Setzer C. N., et al. 2024, *MNRAS*, **531**, 1203

Schröder S. L., MacLeod M., Loeb A., et al. 2020, *ApJ*, **892**, 13

Schroeder G., Ho A. Y. Q., Perley D. A., 2024, Transient Name Server AstroNote, **314**, 1

Schulze S., Krühler T., Leloudas G., et al. 2018, *MNRAS*, **473**, 1258

Schulze S., Fransson C., Kozyreva A., et al. 2024, *A&A*, **683**, A223

Siegel D. M., Agarwal A., Barnes J., et al. 2022, *ApJ*, **941**, 100

Sądowski A., Narayan R., 2015, *MNRAS*, **453**, 3213

Smith P. S., Leonard D. C., Bilinski C., et al. 2018, The Astronomer's Telegram, **11789**, 1

Soker N., 2019, *Science China Physics, Mechanics, and Astronomy*, **62**, 119501

Soker N., 2022, *Research in Astronomy and Astrophysics*, **22**, 055010

Soker N., Grichener A., Gilkis A., 2019, *MNRAS*, **484**, 4972

Somalwar J. J., Ravi V., Margutti R., et al. 2025, arXiv e-prints, p. [arXiv:2505.11597](https://arxiv.org/abs/2505.11597)

Srinivasaraghavan G., Ho A., Perley D., et al. 2024, Transient Name Server AstroNote, **276**, 1

Stein R., van Velzen S., Kowalski M., et al. 2021, *Nature Astronomy*, **5**, 510

Sun N.-C., Maund J. R., Crowther P. A., et al. 2022, *MNRAS*, **512**, L66

Sun N.-C., Maund J. R., Shao Y., et al. 2023, *MNRAS*, **519**, 3785

Suzuki A., Maeda K., 2017, *MNRAS*, **466**, 2633

Suzuki A., Maeda K., 2021, *ApJ*, **908**, 217

Suzuki A., Maeda K., 2022, *ApJ*, **925**, 148

Suzuki A., Irwin C. M., Maeda K., 2024, *PASJ*, **76**, 863

Taddia F., Sollerman J., Fremling C., et al. 2019, *A&A*, **621**, A71

Tanaka M., Maeda K., Mazzali P. A., et al. 2017, *ApJ*, **837**, 105

Tonry J. L., 2011, *PASP*, **123**, 58

Tonry J. L., Denneau L., Heinze A. N., et al. 2018, *PASP*, **130**, 064505

Toshikage S., Kimura S. S., Shimizu N., et al. 2025, arXiv e-prints, p. [arXiv:2504.04741](https://arxiv.org/abs/2504.04741)

Tsuna D., Lu W., 2025, *ApJ*, **986**, 84

Uno K., Maeda K., 2020a, *ApJ*, **897**, 156

Uno K., Maeda K., 2020b, *ApJ*, **905**, L5

Uno K., Maeda K., 2023, *MNRAS*, **521**, 4598

Villar V. A., Berger E., Metzger B. D., et al. 2017, *ApJ*, **849**, 70

Vurm I., Metzger B. D., 2021, *ApJ*, **917**, 77

Wise J., Perley D., Sarin N., et al. 2025, arXiv e-prints, p. [arXiv:2507.07380](https://arxiv.org/abs/2507.07380)

Xiang D., Wang X., Lin W., et al. 2021, *ApJ*, **910**, 42

Yao Y., Ho A. Y. Q., Medvedev P., et al. 2022, *ApJ*, **934**, 104

Zauderer B. A., Berger E., Soderberg A. M., et al. 2011, *Nature*, **476**, 425

van Velzen S., Anderson G. E., Stone N. C., et al. 2016, *Science*, **351**, 62

APPENDIX A: THE PHOTOSPHERE OF A HOMOLOGOUS EXPANDING MEDIUM

One argument against interpretations involving SNe, jets, or other expanding media is the behaviour of the photosphere of AT2024wpp. The photosphere peaks at ~ 5 days, but the spectra suggest that ejecta remains optically thick until $\gtrsim 40$ days (Perley et al. 2026). The timescale between when the photospheric radius peaks and when the ejecta becomes optically thin can be derived using a few simple assumptions and compared to the observed data.

Assume that the ejecta is expanding homologously with a power law density profile $\rho \propto r^{-\alpha}$, where $\alpha \geq 0$. The total mass of the ejecta is M_{ej} and the inner and outer edges of the ejecta are traveling at v_{in} and v_{out} respectively. The opacity κ is assumed to be constant and

the ejecta is assumed to be spherical. The initial size of the object is initially assumed to be small, although we show the effect of relaxing that assumption after.

The photospheric radius R_{phot} can be derived by finding the location where the integrated optical depth from the edge of the ejecta becomes $\sim 2/3$ (Arnett 1980; Arnett & Fu 1989), i.e.

$$2/3 = \int_{R_{\text{phot}}}^{v_{\text{out}}t} \rho(r, t) \kappa dr. \quad (\text{A1})$$

Instead of continuing the derivation for arbitrary α , we instead focus on the two extreme cases, $\alpha = 0$ and $\alpha \rightarrow \infty$.

For $\alpha = 0$, the density is

$$\rho = \frac{3M_{\text{ej}}}{4\pi(v_{\text{out}}^3 - v_{\text{in}}^3)t^3}. \quad (\text{A2})$$

Substituting this into Equation A1 gives

$$2/3 = \int_{R_{\text{phot}}}^{v_{\text{out}}t} \frac{3M_{\text{ej}}\kappa}{4\pi(v_{\text{out}}^3 - v_{\text{in}}^3)t^3} dr, \quad (\text{A3})$$

$$= \frac{3M_{\text{ej}}\kappa}{4\pi(v_{\text{out}}^3 - v_{\text{in}}^3)t^3} (v_{\text{out}}t - R_{\text{phot}}), \quad (\text{A4})$$

so

$$R_{\text{phot}} = v_{\text{out}}t - \frac{8\pi(v_{\text{out}}^3 - v_{\text{in}}^3)t^3}{9M_{\text{ej}}\kappa}. \quad (\text{A5})$$

The timescale for the photosphere to reach a peak is

$$t_{\text{phot,peak}} = \sqrt{\frac{3M_{\text{ej}}\kappa v_{\text{out}}}{8\pi(v_{\text{out}}^3 - v_{\text{in}}^3)}}, \quad (\text{A6})$$

and the timescale when the entire ejecta becomes optically thin ($R_{\text{phot}} = v_{\text{in}}t$) and enters the nebular phase is

$$t_{\text{neb}} = \sqrt{\frac{9M_{\text{ej}}\kappa(v_{\text{out}} - v_{\text{in}})}{8\pi(v_{\text{out}}^3 - v_{\text{in}}^3)}}. \quad (\text{A7})$$

The ratio between these two is

$$\frac{t_{\text{neb}}}{t_{\text{phot,peak}}} = \sqrt{\frac{3(v_{\text{out}} - v_{\text{in}})}{v_{\text{out}}}} \leq \sqrt{3}. \quad (\text{A8})$$

For $\alpha \rightarrow \infty$, the ejecta expands in a thin shell. R_{phot} will increase linearly until the ejecta becomes optically thin, so the ratio $t_{\text{neb}}/t_{\text{phot,peak}} \rightarrow 1$ for this case. Intermediate values of α should show $t_{\text{neb}}/t_{\text{phot,peak}}$ between 1 and $\sqrt{3}$, so the highest this ratio can go within the assumptions we have made is $\sqrt{3}$. Values higher than this indicate that the ejecta is likely highly non-spherical or not expanding homologously, either decelerating strongly, remaining stationary, or having mass continuously injected into the ejecta.

However, if the ejecta has an initial radius of R_0 , then time t in Equation A5 gets replaced with $t + R_0/v_{\text{out}}$, and both $t_{\text{phot,peak}}$ and t_{neb} become smaller by R_0/v_{out} , thus, the ratio between them becomes

$$\frac{t_{\text{neb}}}{t_{\text{phot,peak}}} = \frac{t_{\text{neb}}(R_0=0) - R_0/v_{\text{out}}}{t_{\text{phot,peak}}(R_0=0) - R_0/v_{\text{out}}} > \frac{t_{\text{neb}}(R_0=0)}{t_{\text{phot,peak}}(R_0=0)}. \quad (\text{A9})$$

Thus, an extended progenitor on the order of $R_0 = v_{\text{out}}t_{\text{phot,peak}}(R_0=0)$

can have a high enough ratio to be consistent with observations. However, for AT 2024wpp, this radius is $\gtrsim 10^{15}$ cm, which rules out stars without extended, dense CSM expanding homologously with the ejecta.

This paper has been typeset from a `TeX/LaTeX` file prepared by the author.